Respiratory Physiology & Neurobiology 190 (2014) 54–61

Contents lists available at ScienceDirect

Respiratory Physiology & Neurobiology

journal homepage: www.elsevier.com/locate/resphysiol

Surface mapping for visualization of wall stresses during inhalation in a human nasal cavity

Kiao Inthavong, Yidan Shang, Jiyuan Tu*

School of Aerospace, Mechanical and Manufacturing Engineering, RMIT University, Australia

ARTICLE INFO

Article history:
Received 17 April 2013
Received in revised form 9 September 2013
Accepted 10 September 2013

Keywords:
Surface map
Wall shear stress
Nasal cavity
CFD
Inhalation

ABSTRACT

Airflow analysis can assist in better understanding the physiology however the human nasal cavity is an extremely complicated geometry that is difficult to visualize in 3D space, let alone in 2D space. In this paper, an anatomically accurate 3D surface of the nasal passages derived from CT data was unwrapped and transformed into a 2D space, into a UV-domain (where u and v are the coordinates) to allow a complete view of the entire wrapped surface. This visualization technique allows surface flow parameters to be analyzed with greater precision. A *UV*-unwrapping tool is developed and a strategy is presented to allow deeper analysis to be performed. This includes (i) the ability to present instant comparisons of geometry and flow variables between any number of different nasal cavity models through normalization of the 2D unwrapped surface; (ii) visualization of an entire surface in one view and; (iii) a planar surface that allows direct 1D and 2D analytical solutions of diffusion of inhaled vapors and particles through the nasal walls. This work lays a foundation for future investigations that correlates adverse and therapeutic health responses to local inhalation of gases and particles.

1. Introduction

The fluid dynamics behavior and physical interactions between the surface wall, inhaled air and particles all occur simultaneously during inhalation. Visualization of fluid and particle flow during inhalation can provide insight and a better understanding into the physics involved in respiration. During nasal inhalation, moving air passing over the nasal cavity walls creates a shearing of the fluid producing airflow-induced mechano-physical stress in the form of a wall shear stress (Elad et al., 2006). Recent WSS mapping on surface walls in hemodynamic studies have helped establish causative-effect relations in understanding morphology and risk assessments of aneursyms (Goubergrits et al., 2012; Reneman et al., 2006). Similarly, such mappings can assist in understanding the link between the complex nasal morphology and its physiological functions, which contribute toward many current research fields including nasal surgery (Kim et al., 2013; Rhee et al., 2011), particle inhalation and its toxicology (Inthavong et al., 2009), and physiological function (Elad et al., 2008; Lee et al., 2010).

Doorly et al. (2008) analyzed the effect of flow instability on wall shear stress (WSS), by mapping out the WSS occurring along the perimeter of one cross-sectional slice. The profile was taken along the cross-sectional perimeter slice which means that WSS profiles can only be viewed along the specified slices. Using this method would be difficult in displaying many possible WSS profiles along the perimeter of cross-section slices to map out the entire cavity wall. An alternative is to display a WSS contour over the 3D domain. This would allow a qualitative result that can reveal local concentrated stresses. However the representation of 3D model results is limited to digital media where software is needed to rotate the model to obtain the desired view. Even under this method, not all surfaces can be viewed adequately, with ease.

An alternative is to transform the 3D model into a 2D representation by the *UV* mapping technique used in computer graphics. The letters *U* and *V* denote the coordinate axes of the 2D plane while *X*, *Y*, *Z* are retained in the coordinate axes of the 3D object. The 2D map provides an overview of the entire geometry, where both septal and lateral wall surfaces can be plotted simultaneously – a feature that is prohibitive in 3D models. The *UV* mapping is highly effective for reporting results in 2D format, e.g. paper reports.

Furthermore a recurring theme emerging from recent studies of nasal inhalation (Abouali et al., 2012; Chung and Kim, 2008; Na et al., 2012; Wen et al., 2008; White et al., 2011; Zhu et al., 2011) is the differences found in nasal morphology between individuals which has been attributed to age, sex, and ethnicity (Churchill et al., 2004). Intra-individual differences are also found between the structure of the left and right nasal airways, as well as temporal variations caused by nasal cycling

* Corresponding author at: School of Aerospace, Mechanical, and Manufacturing Engineering, RMIT University, PO Box 71, Bundoora, VIC 3083, Australia.
Tel.: +61 3 9925 6191; fax: +61 3 9925 6108.
E-mail address: jiyuan.tu@rmit.edu.au (J. Tu).

1569-9048/$ – see front matter © 2013 Elsevier B.V. All rights reserved.
http://dx.doi.org/10.1016/j.resp.2013.09.004

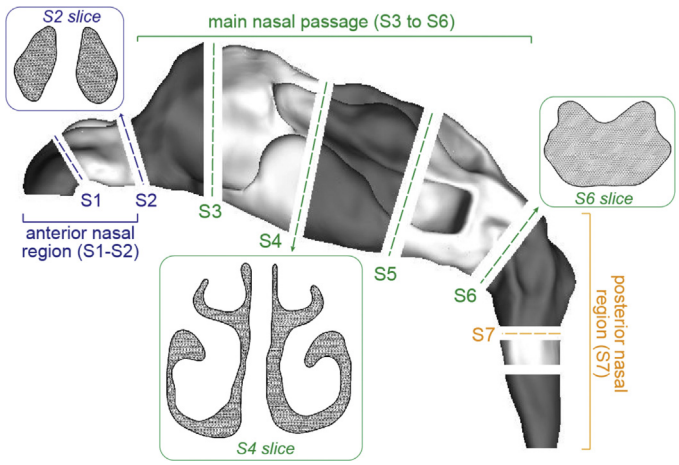

Fig. 1. Nasal cavity geometry with sectioned slices, labeled as S1–S7. Three cross-sections are shown taken at S2, S4, and S6.

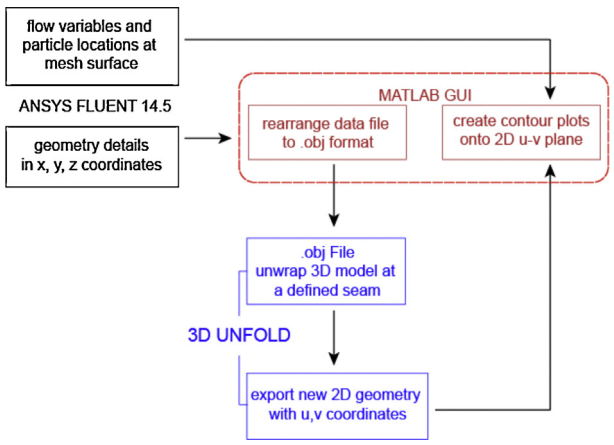

Fig. 2. Flow chart showing the conversion process of a 3D nasal cavity geometry into a 2D surface representation.

(Eccles, 1996). Recently a single representative model of the human nasal cavity was produced by Liu et al. (2009) based on measurements of 30 sets of computed tomography (CT) scans of nasal airways was created, while Gambaruto et al. (2012) presented an averaged geometry using Fourier descriptors and medial axis transforms of cross-sectional slices of three nasal cavities.

In this study, a *UV*-unwrapping strategy and data management and analysis tool is developed to allow new methods of respiratory flow analysis and direct comparisons between different models. The *UV* unwrapping approach allows (i) the ability to present instant comparisons of geometry and flow variables between any number of different nasal cavity models through normalization of the 2D unwrapped surface; (ii) visualization of an entire surface in one view and; (iii) a planar surface for direct 1D and 2D analytical solutions of diffusion of inhaled vapors and particles through the sub-nasal walls. An executable program for data management and analysis is developed as part of the unwrapping methodology and this is available online at www.cfdresearch.com/matlab-2/uv-unwrapping-tool/. This work lays a foundation for future investigations that incorporates toxicology and health responses to local inhalation of gases and particles by creating additional *UV*-layers underneath the unwrapped surface map that represents the sub-nasal wall layers, e.g. mucus, tissue, and blood layers.

2. Method

2.1. Computational model

A computational fluid dynamics (CFD) model of a human nasal cavity obtained through CT scans from a healthy 25-year old, Asia male (170 cm height, 75 kg mass) has been created (Inthavong et al., 2011a) and for brevity the details of its model construction and verification can be found in Inthavong et al. (2009) and Wen et al. (2008). Grid independence was tested and the mesh was refined in the near wall and regions of high curvature. The nasal cavity was meshed with unstructured tetrahedral cells (3.7 million cells, 318 MB in computational memory size) with 10 prism layers attached on the wall using a HPxw6600 16 Gb RAM, 8 processor workstation. For turbulent flow regimes, typically for flow rates greater than 20 L/min the maximum y^+ value was in the order of 10^{-1} ($y^+_{max} = 0.48$).

The computational model was divided into eight sections, by seven slices and labeled as S1–S7 (Fig. 1). The regions S1 and S2 are contained in the anterior third with S2 slicing through the nasal valve region, S3–S6 are in the main nasal passage which displays the turbinate intrusions into the airway and the well-defined septal walls, while S7 is in the posterior third containing the airway curvature into the nasopharynx. Two straight extension pipes, one at the inlet, and one at the outlet were created into the geometry to satisfy a fully developed flow assumption, each having a length of ten times its diameter.

2.2. UV-unwrapping

The flow process of converting a 3D model to 2D surface is outlined in a flow chart given in Fig. 2. The data containing information regarding the 3D nasal cavity geometry from Ansys-Fluent CFD commercial software is outputted as an *ascii* file format and accessed through Matlab. The data is rearranged so that it conforms to the .obj file format. This allows the data to be read into an open source (Blender, Blender Foundation) or commercial (3D Unfold, Polygonal Design, France) 3D modeling software. Within the software, the 3D model is unwrapped at a defined seam based on the ISOMAP algorithm (Tenenbaum et al., 2000). The converted 2D geometry with new coordinates in the *U–V* domain is exported back into Matlab and is coupled with solution data obtained from CFD in the form of the flow variables and particle deposition. A Matlab graphical use interface (GUI) is developed as shown in Fig. 3 to act as an intermediary function to couple the two separate sets of data.

Graphically Fig. 4 presents the flow process. First the nasal cavity is divided into the left and right chambers. Each chamber is then unwrapped by creating a cutting slice along the bottom of the geometry to create a common reference boundary in which the surface coordinates can be related to. This common boundary edge is separated by the inlet and outlet of the nasal chamber. Furthermore the selection of the nasal floor ensures correct topology in the *UV*-domain for regions of overlapping geometry such as that found in the meatus airway.

2.3. Flow modeling and boundary conditions

The geometry and mesh were inputted into a commercial CFD software, Ansys-Fluent v14.5, where the governing equations for fluid flow were modeled, to simulate the steady flow field in nasal

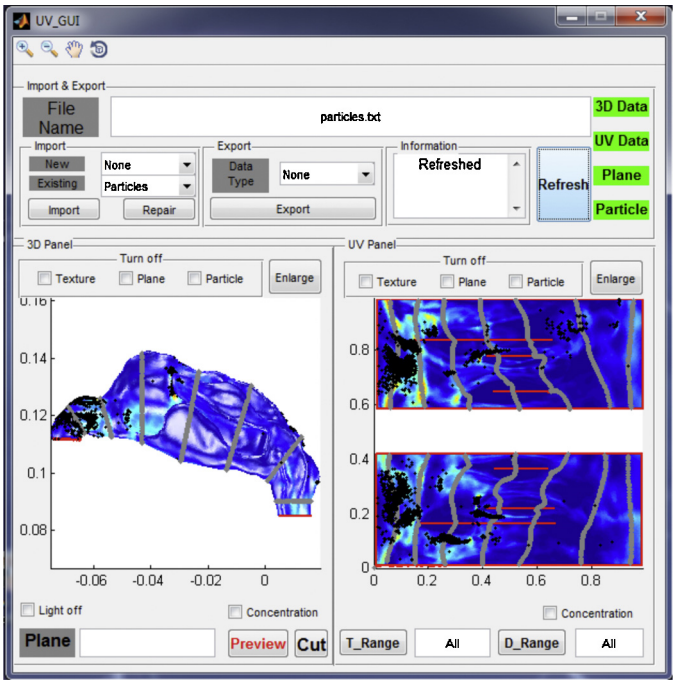

Fig. 3. Developed GUI of Matlab program to read in the CFD and 2D-model geometry data. This tool is available online at www.cfdresearch.com/matlab-2/uv-unwrapping-tool/.

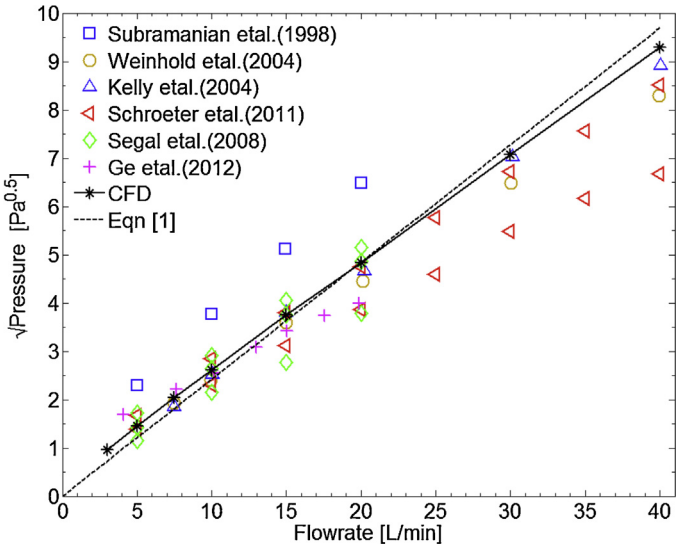

Fig. 5. Pressure drop in a nasal cavity model between the CFD predicted results and recent experimental and numerical data in the literature. The regression line for the CFD predicted is represented by $\sqrt{\Delta P} = 0.225Q + 0.338$, while using Eq. (3) produces $\sqrt{\Delta P} = 0.24245Q$.

cavity. Inhaled air through the nasal cavity is induced by a pressure drop between nostril and lung caused by the movement of the diaphragm. The inlet has a pressure boundary condition set to zero gauge pressure to mimic the ambient surrounding environment. To simulate flow patterns of different flow rates, the outlet was set with the required negative pressure to induce a given flow rate. Experimental work by Hahn et al. (1993) and Kelly et al. (2000), and numerical simulations by Keyhani et al. (1997) have suggested laminar flows up to a rate of 24 L/min. In this study, a laminar flow field was adopted for the flow rates 3–15 L/min, and transitional SST turbulence model was chosen for flow rates 20–40 L/min. For brevity the flow modeling equations can be found in software manual (Ansys, 2007), and the model setup and its verification for this specific nasal cavity model has been reported in Wen et al. (2008) and Inthavong et al. (2011b).

3. Results and discussion

3.1. Pressure drop comparisons

The pressure difference taken between the nostril inlet and nasal pharynx was obtained at flow rates from 3 L/min to 40 L/min with the corresponding Reynolds numbers of 527–7022, where the characteristic length is based on an averaged hydraulic diameter over fourteen cross-sections throughout the airway. The simulated results of the pressure drop between the nostril inlets and the posterior nasal wall at the nasopharynx for different inhalation rates are shown in Fig. 5 where good agreement with the literature is found especially at flow rates less than 20 L/min, where a laminar flow regime is applied. By taking the square root of the pressure

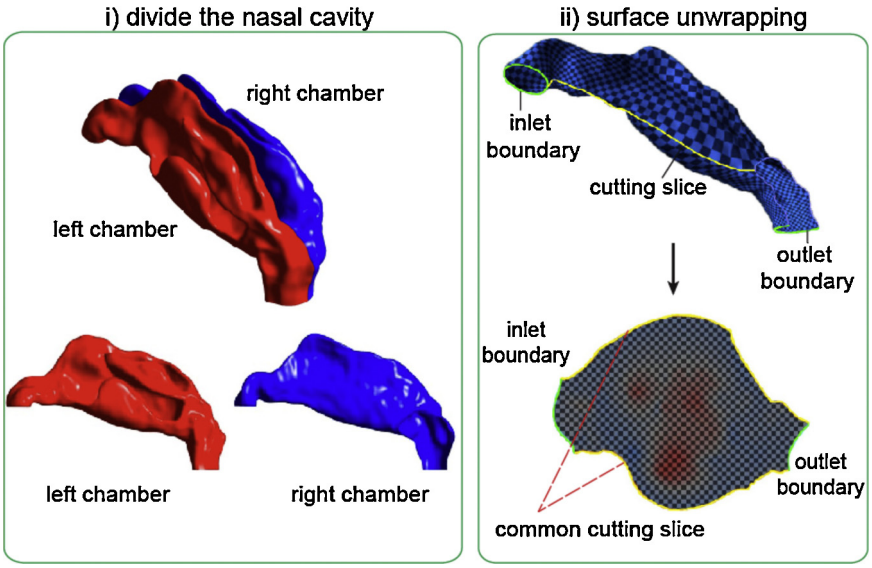

Fig. 4. Flow process in unwrapping the surface of a 3D model into a 2D domain. Characteristic lines are defined at the apex of the septum wall, middle meatus, and inferior meatus.

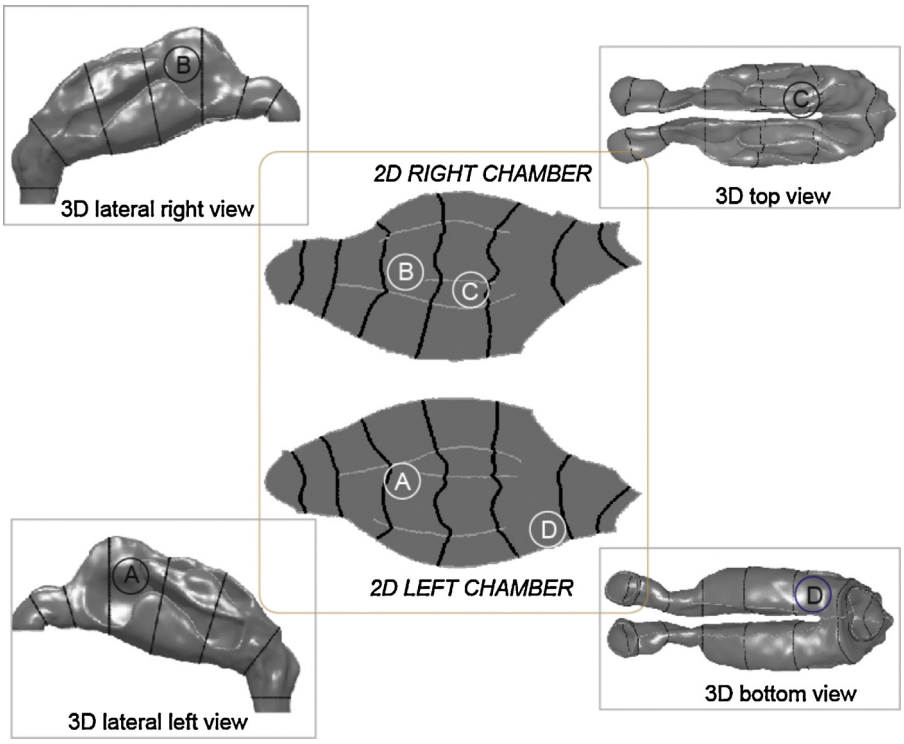

Fig. 6. Identification of four specific locations, A, B, C, D located on nasal cavity 1 (NC1 model) that can be viewed simultaneously in 2D space, but requires four different perspective views in 3D space.

drop, the flow rate and simulated CFD results can be represented by a curve fit:

$$\sqrt{\Delta P} = 0.225Q + 0.338 \quad (1)$$

where Q is the flow rate in L/min.

Since the pressure curve versus flow rate should converge at the origin (0,0) but does not in Eq. (1), an alternative relationship with the airway geometry, flow rate, and pressure drop can be applied if we first assume the following Bernoulli's equation:

$$\frac{P_1}{\rho g} + \frac{u_1^2}{2g} + h_1 = \frac{P_2}{\rho g} + \frac{u_2^2}{2g} + h_2 \quad (2)$$

where ρ is the density of air and g is gravitational acceleration. Neglecting the small difference in height, h_1 and h_2, the pressure drop can be recast as:

$$P_2 - P_1 = \frac{1}{2}\rho(u_1^2 - u_2^2) \quad (3)$$

Bernoulli's principle is valid for inviscid flows only and therefore an averaged velocity parameter is used in place of the velocity difference caused by viscosity in the complex nasal cavity geometry. Replacing the velocity with an overall volume flow rate with a cross-sectional area term:

$$\Delta P = \frac{1}{2}\rho\frac{Q^2}{A_{ave}^2}$$

where Q is the flow rate is normally given in the literature as L/min, A_{ave} is the averaged cross-sectional area. However since the units of velocity (m/s) are different to the flow rate units, then a conversion factor of $1/(36.0 \times 10^4)$ reflects the change in dimensions is used. Then taking the square root of the function, the equation becomes

$$\sqrt{\Delta P} = \frac{1}{A_{ave}(6.0 \times 10^4)}\sqrt{\frac{1}{2}\rho}Q = kQ \quad (4)$$

and k can be treated as a constant equal to $1/(A_{ave}(6.0 \times 10^4))\sqrt{(1/2)\rho}$.Since the cross-sectional area varies throughout the flow domain, an averaged value is calculated by taking fourteen slices perpendicular to the curved airway (additional slices distributed in between each of the slices S1–S7 shown in Fig. 1). Integration of each slice over each interval distance is performed and then averaged, resulting in $A_{ave} = 5.38 \times 10^{-5}$ m^2. The constant k from Eq. (4) is then equal to 0.24245, which is the gradient of the curve fit to predict the pressure drop.

One limitation of Eq. (4) is that it is in the form $\Delta P \sim Q^b$, where b is a power of 2 while experimental studies in the literature have reported values of 1.76–1.87 for adults (Garcia et al., 2009), and 1.91 for infants (Golshahi et al., 2010). Another limitation of Eq. (4) is that most data in Fig. 5 come from CFD studies. In vivo, wall compliance may result in a pressure–flow relationship that departs from the $\Delta P \sim Q^b$ proportionality predicted by Eq. (4).

3.2. Visualization and geometry normalization the nasal cavity

In 3D space the nasal cavity can be portrayed from one perspective view only. This limits the ability to inspect specific regions that may not lay on the same surface. Specifically Fig. 6 demonstrates the ability of the *UV*-unwrapping to define four specific locations, namely *A*, *B*, *C*, and *D* with one view in 2D space rather than four views required in 3D space.

A single view of the entire surface allows direct comparisons left and right chambers and also local regions of any fluid flow variables or particle deposition patterns that occur on the surface. While this can be achieved in 3D space, rotation, and surface transparency or culling is needed to visualize regions that are hidden behind anatomical structures, such as the meatus passage.

The *UV*-unwrapping allows direct comparisons between the left and right chambers of the nasal cavity which exhibit geometry differences due to nasal cycling, mucus secretion, and other physiological response to the external environment. Further variations

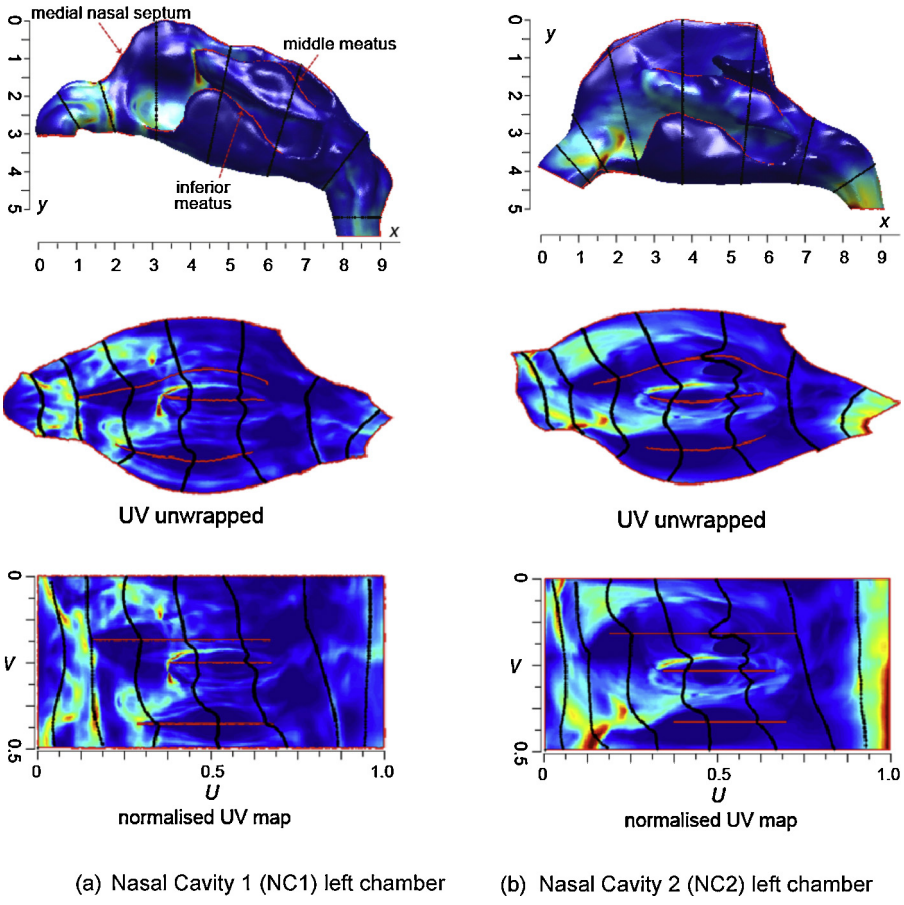

Fig. 7. Normalization of the coordinates *U* and *V* of the two different nasal cavities (NC1 and NC2) that have been unwrapped. Three characteristic lines, *medial nasal septum*, *middle meatus*, and *inferior meatus* serving as visual markers are shown in (a) nasal cavity 1 (NC1) model.

can be found between individual nasal cavity geometries due to sex, race, and age. For direct comparisons to be made in this case, the *UV*-unwrapped surface needs to be normalized in its *U* and *V* coordinates. Fig. 7 shows two nasal cavities, namely NC1 [nasal cavity 1 found in Wen et al. (2008 #18)] and NC2 [nasal cavity 2 found in Ge et al. (2012 #40)] which exhibit geometric differences. Three characteristic lines, serving as visual markers, are created based on the ceiling of the meatus boundaries. These lines are the *medial nasal septum* line that separates the septum and the lateral sides; the *middle meatus* which is the middle line and is the shortest, and;

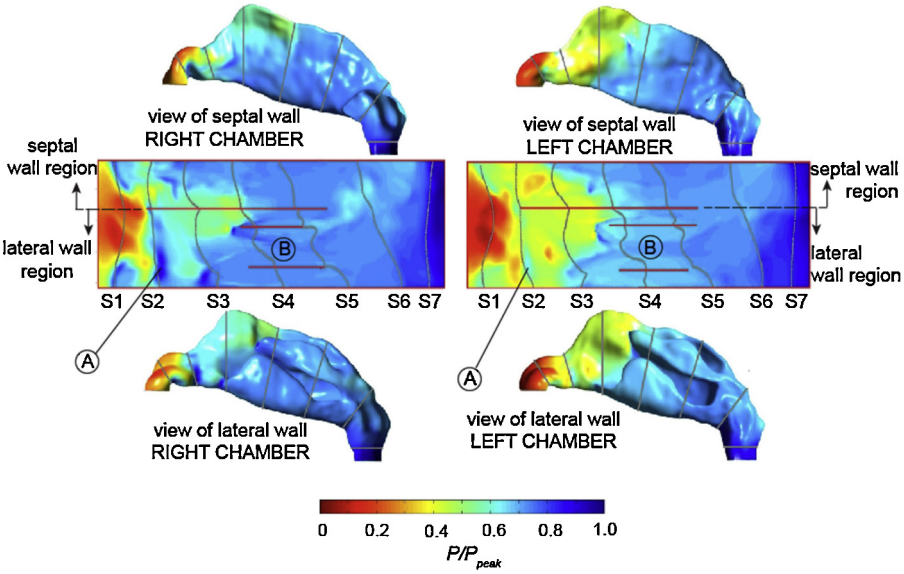

Fig. 8. Surface pressure distribution mapping from a 3D model to the 2D *UV*-plane for an inspiratory flow rate 10 L/min. $P_{peak} = -5$ Pa. The three red lines running in the axial direction are the characteristic lines defined in Fig. 6. Local regions labeled as 'A' and 'B' are local minimum or low pressure that is surrounded by higher pressure values.

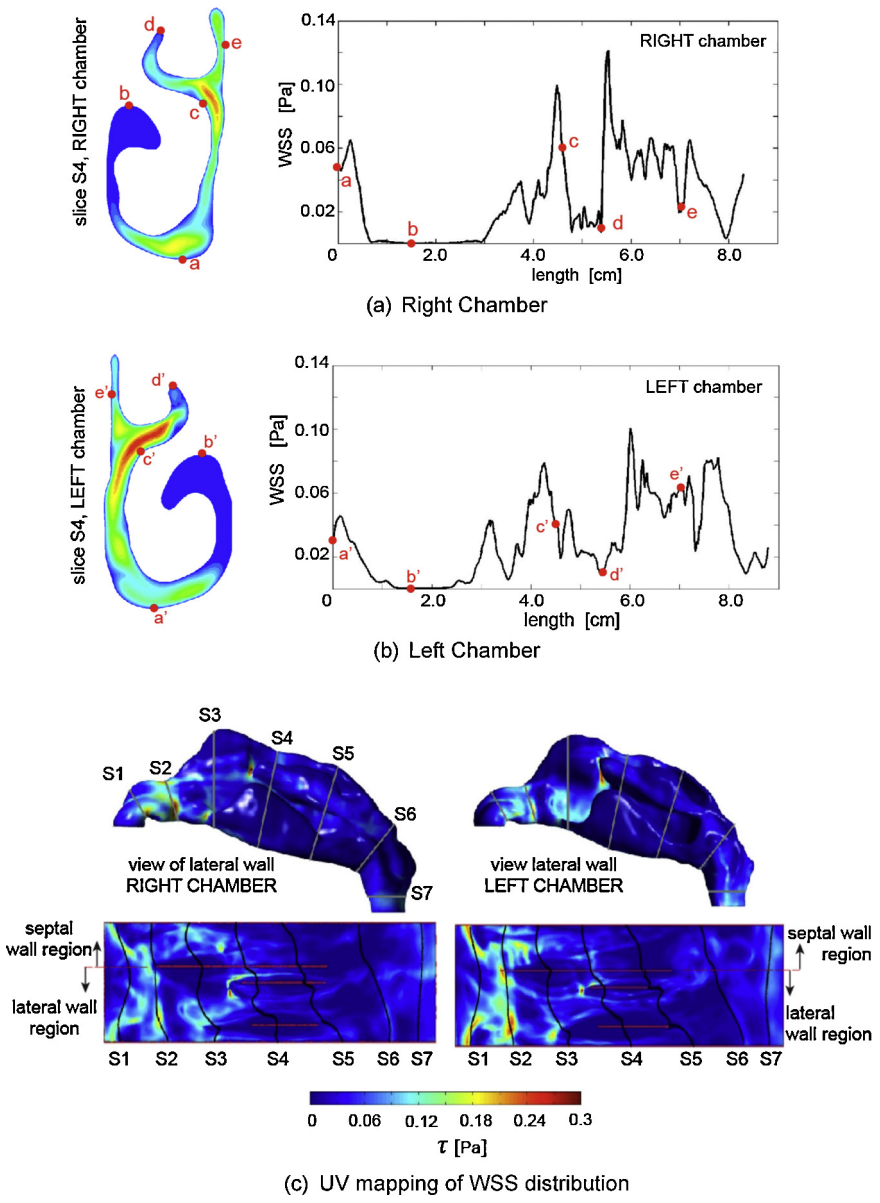

Fig. 9. (a) Velocity magnitude contour map for an inspiratory flow rate 10 L/min on the cross-section slice S4 and its circumferential WSS profile for the (a) right chamber and (b) left chamber. (c) *UV* mapping technique to display the shear stress distribution mapping from a 3D model to the 2D-plane.

the *inferior meatus* which is closest to the floor of the main nasal passage, and hence its position close to the cutting slice shown in Fig. 4.

From the unwrapped surfaces some of the differences include the nostril shape, turbinate intrusions, and nasopharynx curvature. Normalization of the *U* and *V* coordinate produces a map that shares the same extents between the two inherently different geometries. The normalized *UV* map shows that the middle meatus in NC1 is closer to the medial nasal septum line while the NC2 model shows a more even distance between the three characteristic lines. The normalized *UV* map provides a means direct comparisons between individual nasal cavity geometries and also for identifying persistent flow features despite differences in geometries.

3.3. Applications of UV-unwrapped surface

3.3.1. Pressure distribution mapping

The results from a flow rate of 10 L/min are presented to reflect typical flow behavior and patterns arising from a low inhalation or breathing rate. Fig. 8 shows the pressure contour on the nasal cavity walls of the right and left chambers in 3D and in the *UV*-domain. In general, the pressure distribution decreases smoothly along the nasal cavity from nostril to nasal pharynx. The rate of decrease differs between each chamber due to the differing asymmetrical geometries caused by the nasal cycle. During CT scanning one nasal chamber is usually more patent than the other as a result of congestion (swelling) of the erectile tissue (cavernous tissues of the mucosa) while at the same time decongestion (shrinking) occurs to the erectile tissue in the other chamber (Eccles, 1996). The pressure distribution is then influenced by the resistance caused by the geometry of each chamber.

The differences in geometry between the left and right nasal chambers can be seen from the *UV*-domain where there is higher pressure in the region between nostril and slice S4 in the left chamber. For each chamber, the high-pressure regions are found at the upper regions of S1 and S2 which is due to the air flow velocity turning from a vertical to horizontal direction.

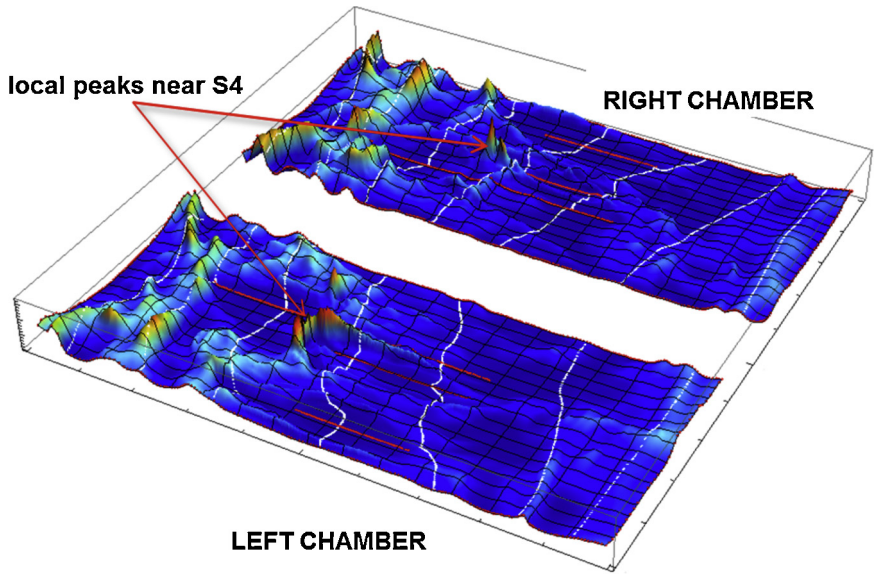

Fig. 10. Local peaks, identified with the red arrows, are found near slice S4. The three red lines running in the axial direction are the characteristic lines defined in Fig. 4.

The nasal valve region is the region that contains the minimum cross-sectional area where the flow accelerates through a converging passageway before decelerating as the flow diverges outwards. This flow phenomenon is characterized by an acceleration in the inhaled air as the passageway narrows, before deceleration through the increase in the cross-sectional area of the passageway. Correspondingly the pressure prior to the minimum cross-sectional area must exhibit a negative pressure gradient, leading to a local minimum pressure as the flow accelerates, and then produce a positive pressure gradient leading to an increase in the pressure again as the flow decelerates. This region is labeled as 'A' which can be seen in the vicinity of the S2 slice line where a local minimum or lower pressure is found surrounded by higher pressure values. As the flow enters the turbinate region, the surface walls caused by the indentation of the middle turbinates cannot be typically visualized in 3D since it is sheltered from view. These surface walls in the *UV*-domain are labeled as 'B', which is the region between the inferior and middle meatus characteristic lines. After the S4 slice the flow begins to recover from the divergence in spatial volume in the main nasal passage. The pressure becomes more uniform just prior to the inhaled air from both left and right chambers merge at S6.

3.4. WSS distribution mapping

Perimeter WSS profiles in the middle turbinate region at the S4 slice are shown for the right and left chamber in Fig. 9a and b respectively. The bulk fluid flow remains close to the septal wall and splits into two local regions – one superiorly located near the meatus bifurcation, and one inferiorly located near the floor of the nasal passage. Local WSS peaks in the perimeter profile, correlate with the flow field and is a good indicator of the bulk flow distribution. The perimeter profile technique provides highly detailed WSS distribution over the surface of a cross-section, but requires a substantial number of slices to capture the entire 3D domain.

The WSS distribution in 3D and its conversion into the *UV*-space is given in Fig. 9c. Using this technique the entire wall surface can be displayed in one image. In the literature, maximum shear stresses have been found in the range of 0.2 Pa (Elad et al., 1993) on the septal wall across the inferior turbinate at a peak inspiration of 20 L/min. Comparatively, the stresses in uniform regions of large arteries are in the range of 1.5–2 Pa (Nucci et al., 2003). Under a flow rate of 10 L/min local peaks of approximately 0.3 Pa are found in the region between the middle meatus and lateral wall in both chambers. Interestingly other local peaks are found only in the anterior region of each chamber, e.g. region before S4. In particular high shear stresses are found on slices 1 and 2 on both the lateral and septal sides. This suggests the inhaled air disperses laterally and shears across the side walls of each chamber as it enters the nasal vestibule. As shear stresses are linearly related to the local velocity, these values significantly increase as breathing efforts increase. High shear stresses that are concentrated locally may also cause irritation of the blood vessels within that area.

Using the *UV*-domain, the WSS can be visualized with 3D peaks to highlight the distribution over the surface wall. This visualization is shown in Fig. 10 where along each of the three characteristic lines (red lines), the WSS was found to be close to zero. These lines are located at the roof of each of the inferior, middle meatus and the main nasal passages where very low flows exist. The surrounding WSS distribution around this near zero region is also void of many high WSS regions which suggests that the inhaled air passing through the middle section of the nasal airway is smoother and stable than that occurring in the anterior half of the nasal chambers. By mapping out the distribution of the stresses on the nasal cavity walls, insight into the mechanoreceptor response can be predicted.

4. Conclusion

A nasal cavity model in 3D space was transformed into a 2D space, namely the *UV*-domain. Using this visualization technique, flow parameters along the surface wall that is typically difficult to visualize and analyze can be presented to provide a deeper insight into the physiological mechanisms involved with respiratory airflows. The pressure distribution was mapped onto the *UV*-domain which showed a higher resistance in the anterior regions of the left nasal chamber, suggesting that the geometry is susceptible to impediment to flow. This may be in the form of a more narrowed geometry, high curvatures or regions leading to flow separation. Wall shear stresses, which lead to mechano-physical responses in the epithelium surfaces, are mapped which revealed the most vulnerable regions in the form of peaks occurring in the anterior nasal chambers and at the entrance of the middle meatus passageway. This mapping technique allows precise predictions of local regions that are disposed to high shearing which is not possible in 3D. The visualization technique presented can be used to make direct

comparisons for different shaped geometries by normalizing each *UV*-mapped geometry. Extension to multiple models can be performed following the flow process presented in the methodology. In this study, a visualization technique is presented that takes a 3D wrapped surface and maps it onto a 2D *UV*-domain, which extends the current CFD technology and capability in visualizing the fluid flow dynamics and particle deposition patterns.

Acknowledgements

The authors would like to gratefully acknowledge the financial support provided by the Australian Research Council (Project ID: DP120103958), and the assistance of resources provided at the NCI National Facility Systems at the Australian National University through the National Computational Merit Allocation Scheme supported by the Australian Government.

References

Abouali, O., Keshavarzian, E., Farhadi Ghalati, P., Faramarzi, A., Ahmadi, G., Bagheri, M.H., 2012. Micro and nanoparticle deposition in human nasal passage pre and post virtual maxillary sinus endoscopic surgery. Respiratory Physiology & Neurobiology 181, 335–345.

Ansys, 2007. Fluent User Manual. Ansys Inc., USA.

Chung, S.-K., Kim, S.K., 2008. Digital particle image velocimetry studies of nasal airflow. Respiratory Physiology & Neurobiology 163, 111–120.

Churchill, S., Shackelford, L.L., Georgi, N., Black, M., 2004. Morphological variation and airflow dynamics in the human nose. American Journal of Human Biology 16, 625–638.

Doorly, D.J., Taylor, D.J., Schroter, R.C., 2008. Mechanics of airflow in the human nasal airways. Respiratory Physiology & Neurobiology 163, 100–110.

Eccles, R., 1996. A role for the nasal cycle in respiratory defence. European Respiratory Journal 9, 371–376.

Elad, D., Liebenthal, R., Wenig, B.L., Einav, S., 1993. Analysis of air flow patterns in the human nose. Medical & Biological Engineering & Computing 31, 585–592.

Elad, D., Naftali, S., Rosenfeld, M., Wolf, M., 2006. Physical stresses at the air–wall interface of the human nasal cavity during breathing. Journal of Applied Physiology 100, 1003–1010.

Elad, D., Wolf, M., Keck, T., 2008. Air-conditioning in the human nasal cavity. Respiratory Physiology & Neurobiology 163, 121–127.

Gambaruto, A.M., Taylor, D.J., Doorly, D.J., 2012. Decomposition and description of the nasal cavity form. Annals of Biomedical Engineering 40, 1142–1159.

Garcia, G.J.M., Tewksbury, E.W., Wong, B.A., Kimbell, J.S., 2009. Interindividual variability in nasal filtration as a function of nasal cavity geometry. Journal of Aerosol Medicine and Pulmonary Drug Delivery 22, 139–155.

Ge, Q.J., Inthavong, K., Tu, J.Y., 2012. Local deposition fractions of ultrane particles in a human nasal-sinus cavity CFD model. Inhalation Toxicology 24 (8), 492–505.

Golshahi, L., Finlay, W.H., Olfert, J.S., Thompson, R.B., Noga, M.L., 2010. Deposition of inhaled ultrafine aerosols in replicas of nasal airways of infants. Aerosol Science and Technology 44, 741–752.

Goubergrits, L., Schaller, J., Kertzscher, U., van den Bruck, N., Poethkow, K., Petz, C., Hege, H.C., Spuler, A., 2012. Statistical wall shear stress maps of ruptured and unruptured middle cerebral artery aneurysms. Journal of the Royal Society Interface 9, 677–688.

Hahn, I., Scherer, P.W., Mozell, M.M., 1993. Velocity profiles measured for airflow through a large-scale model of the human nasal cavity. Journal of Applied Physiology 75, 2273–2287.

Inthavong, K., Ge, Q., Se, C.M.K., Yang, W., Tu, J.Y., 2011a. Simulation of sprayed particle deposition in a human nasal cavity including a nasal spray device. Journal of Aerosol Science 42, 100–113.

Inthavong, K., Tu, J.Y., Ahmadi, G., 2009. Computational modelling of gas-particle flows with different particle morphology in the human nasal cavity. Journal of Computational Multiphase Flows 1, 57–82.

Inthavong, K., Zhang, K., Tu, J., 2011b. Numerical modelling of nanoparticle deposition in the nasal cavity and the tracheobronchial airway. Computer Methods in Biomechanics and Biomedical Engineering 14, 633–643.

Kelly, J.T., Prasad, A.K., Wexler, A.S., 2000. Detailed flow patterns in the nasal cavity. Journal of Applied Physiology 89, 323–337.

Keyhani, K., Scherer, P.W., Mozell, M.M., 1997. A numerical model of nasal odorant transport for the analysis of human olfaction. Journal of Theoretical Biology 186, 279–301.

Kim, S.K., Na, Y., Kim, J.-I., Chung, S.-K., 2013. Patient specific CFD models of nasal airflow: overview of methods and challenges. Journal of Biomechanics 46, 299–306.

Lee, J.-H., Na, Y., Kim, S.-K., Chung, S.-K., 2010. Unsteady flow characteristics through a human nasal airway. Respiratory Physiology & Neurobiology 172.

Liu, Y., Johnson, M.R., Matida, E.A., Kherani, S., Marsan, J., 2009. Creation of a standardized geometry of the human nasal cavity. Journal of Applied Physiology 106, 784–795.

Na, Y., Chung, K.S., Chung, S.-K., Kim, S.K., 2012. Effects of single-sided inferior turbinectomy on nasal function and airflow characteristics. Respiratory Physiology & Neurobiology 180, 289–297.

Nucci, G., Suki, B., Lutchen, K., 2003. Modeling airflow-related shear stress during heterogeneous constriction and mechanical ventilation. Journal of Applied Physiology 95, 348–356.

Reneman, R.S., Arts, T., Hoeks, A.P., 2006. Wall shear stress – an important determinant of endothelial cell function and structure – in the arterial system in vivo. Discrepancies with theory. Journal of Vascular Research 43, 251–269.

Rhee, J.S., Pawar, S.S., Garcia, G.J., Kimbell, J.S., 2011. Toward personalized nasal surgery using computational fluid dynamics. Archives of Facial Plastic Surgery 13, 305–310.

Tenenbaum, J.B., Silva, V. d., Langford, J.C., 2000. A global geometric framework for nonlinear dimensionality reduction. Science 290, 2319–2323.

Wen, J., Inthavong, K., Tu, J.Y., Wang, S., 2008. Numerical simulations for detailed airflow dynamics in a human nasal cavity. Respiratory Physiology & Neurobiology 161, 125–135.

White, D.E., Al-Jumaily, A.M., Bartley, J., Lu, J., 2011. Correlation of nasal morphology to air-conditioning and clearance function. Respiratory Physiology & Neurobiology 179, 137–141.

Zhu, J.H., Lee, H.P., Lim, K.M., Lee, S.J., Wang, D.Y., 2011. Evaluation and comparison of nasal airway flow patterns among three subjects from Caucasian, Chinese and Indian ethnic groups using computational fluid dynamics simulation. Respiratory Physiology & Neurobiology 175, 62–69.